Comparative numerical-experimental analysis of the universal impact of arbitrary perturbations on transport in three-dimensional unsteady flows

F. Wu,[1] M. F. M. Speetjens,[2,*] D. L. Vainchtein,[1,3] R. R. Trieling,[4] and H. J. H. Clercx[4]

[1]*Department of Mechanical Engineering, Temple University, Philadelphia, Pennsylvania 19122, USA*

[2]*Energy Technology Laboratory, Department of Mechanical Engineering, Eindhoven University of Technology, Eindhoven, The Netherlands*

[3]*Space Research Institute, Moscow, Russia*

[4]*Fluid Dynamics Laboratory, Department of Applied Physics, Eindhoven University of Technology, Eindhoven, The Netherlands*

(Received 17 July 2014; published 8 December 2014)

Numerical studies of three-dimensional (3D) time-periodic flow inside a lid-driven cylinder revealed that a weak perturbation of the noninertial state (Reynolds number $\mathrm{Re} = 0$) has a strong impact on the Lagrangian flow structure by inducing transition of a global family of nested spheroidal invariant surfaces into intricate coherent structures consisting of adiabatic invariant surfaces connected by tubes. These tubes provide paths for passive tracers to escape from one invariant surface to another. Perturbation is introduced in two ways: (i) weak fluid inertia by nonzero $\mathrm{Re} \sim O(10^{-3})$; (ii) small disturbance of the external flow forcing. Both induce essentially the same dynamics, implying a universal response in the limit of a weak perturbation. Moreover, we show that the motion inside tubes possesses an adiabatic invariant. Long-term experiments were conducted using 3D particle-tracking velocimetry and relied on experimental imperfections as natural weak perturbations. This provided first experimental evidence of the tube formation and revealed close agreement with numerical simulations. We experimentally validated the universality of the perturbation response and, given the inevitability of imperfections, exposed the weakly perturbed state as the true "unperturbed state" in realistic systems.

DOI: 10.1103/PhysRevE.90.063002 PACS number(s): 47.10.Fg, 47.52.+j, 47.80.Cb, 47.54.De

I. INTRODUCTION

The scope of the present study is transport phenomena in three-dimensional (3D) unsteady deterministic flows. This is motivated by the still limited insight into this matter, despite its relevance to numerous systems in both nature and industry. Important classes of realistic deterministic flows are laminar flows and averaged or Euler-flow representations of turbulent flows (e.g., Reynolds-Averaged Navier-Stokes equations [1]). Examples encompass a large range of length and time scales and range from geophysical and oceanographical flows [2,3] via industrial fluids processing [4,5] to advanced microfluidic systems [6–8].

In our study we investigated transport in terms of coherent structures formed by the Lagrangian trajectories of tracers that are passively advected by the flow. This "Lagrangian flow structure" geometrically restricts and guides the tracer dispersion and thus determines the transport properties of the flow. This ansatz has found widespread and successful applications in studies of chaotic tracer advection (the kinematic mechanism underlying efficient distributive mixing) [9–13].

We concentrate specifically on qualitative changes in the 3D transport properties due to bifurcations in the Lagrangian flow structure induced by very weak perturbations. To this end, we adopt the 3D time-periodic flow inside a lid-driven cylinder according to [13–17] as a representative experimentally realizable system. Numerical studies of this configuration exposed remarkable responses of the Lagrangian flow structure of the stroboscopic map in the Stokes limit ($\mathrm{Re} = 0$) to minute inertial perturbations [$\mathrm{Re} \sim O(10^{-3}$–$10^{-2})$]: transition of a global family of nested spheroidal invariant surfaces to intricate coherent structures, each formed by merger of (remnants of) two spheroids and one tube, embedded in chaos [13,16,17]. Observations of a similar behavior in a completely different system, an external 3D time-periodic flow driven by a rotating sphere, strongly suggest this is a universal phenomenon [18]. The tube structure is closely related to the capture into resonances in 3D steady and unsteady flows [19–22].

The study below aims at deepening the understanding of the impact of weak perturbations on 3D transport by addressing the following aspects. First, we further explore the degree of universality by investigating whether the observed dynamics can be induced in the 3D cylinder flow through perturbations other than fluid inertia. Second, we further unravel the mechanisms underlying tube formation. The studies in [13,16–18] put forth emergence of certain types of isolated periodic points as a trigger for this phenomenon. However, the fundamental question of whether the tubes are merely individual spiraling orbits or indeed, as conjectured in [16], constitute distinct coherent structures parametrized by a (local) adiabatic invariant remains open. We employ methods proposed in [10,23,24] to investigate this. Third, we further experimentally analyze and validate the observed tracer dynamics and formation of coherent structures by the way of 3D particle-tracking velocimetry (3D-PTV). This expands on earlier experimental studies on the current system in [15,25].

The paper is organized as follows. Section II defines the system and introduces different ways of perturbation. The experimental setup is elaborated in Sec. III. Section IV provides a theoretical-numerical analysis on the response of the Lagrangian flow structure of the unperturbed flow to perturbation. Experimental analysis of observed behavior is carried out in Sec. V. Conclusions are drawn in Sec. VI.

*Corresponding author: m.f.m.speetjens@tue.nl

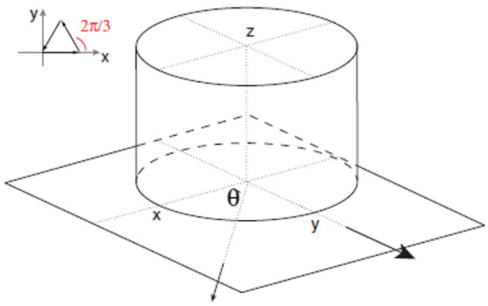

FIG. 1. (Color online) Schematic of the flow forcing by piecewise steady translation of the bottom wall. (Inset) Trajectory of the bottom wall in the three-step forcing protocol adopted in this study. (Adapted from [25].)

II. PROBLEM STATEMENT

A. Flow configuration

In this study, we considered 3D flows inside a cylinder of radius R and height $H = 2R$, driven by the motion of the bottom wall (Fig. 1). The motion of the bottom wall follows a sequence of piecewise steady translations according to a prescribed time-periodic forcing protocol to be specified in Sec. II C. At each forcing step, the bottom wall translates at a velocity u_{wall} over a distance D_{wall} in direction θ_{step} with respect to the x axis. Similar to [25], the present study is restricted to highly viscous fluids, yielding very small diffusion time scales $T_\nu = R^2/\nu$ and rendering the unsteady transient time during the switchings between forcing directions negligible, i.e., $T_\nu/T_{\text{step}} = R^2/\nu T_{\text{step}} \ll 1$, with $T_{\text{step}} = D_{\text{wall}}/u_{\text{wall}}$ the duration of each forcing step. Thus the stepwise flow $\mathbf{u}$ is effectively governed by the steady incompressible Navier-Stokes equations, reading

$$\nabla \cdot \mathbf{u} = 0, \quad \text{Re}\mathbf{u} \cdot \nabla \mathbf{u} = -\nabla p + \nabla^2 \mathbf{u}, \tag{1}$$

in a nondimensional form relative to the unit cylinder $\mathcal{C}$: $[r,\theta,z] = [0,1] \times [0,2\pi] \times [-1,1]$ in cylindrical coordinates. The nondimensional system is parametrized by two nondimensional numbers: the Reynolds number $\text{Re} = u_{\text{wall}} R/\nu \ll 1$ and the nondimensional wall displacement at each forcing step $D = D_{\text{wall}}/R$.

B. Velocity boundary conditions

No-slip velocity conditions $\mathbf{u} = \mathbf{0}$ are imposed on the top wall and cylinder wall; condition $\mathbf{u} = \mathbf{u}_{\text{wall}}$ is imposed on the translating bottom wall, with $u_{\text{wall},x} = u_{\text{wall}} \cos\theta_{\text{step}}$, $u_{\text{wall},y} = u_{\text{wall}} \sin\theta_{\text{step}}$, and $u_{\text{wall},z} = 0$. Two kinds of translation velocities u_{wall} are employed: rigid-wall conditions $u_{\text{wall}} = 1$ and smooth conditions $u_{\text{wall}} = (1 - r^2)^2$. The rigid-wall conditions occur in the real system and have been incorporated in the analytical solution for the Stokes limit, $\text{Re} = 0$; see [26]. However, the discontinuity of the rigid-wall conditions at the bottom rim $(r,z) = (1, -1)$ deteriorates the convergence of the spectral flow solver developed for the simulations of the inertial case, $\text{Re} > 0$ [27]. Utilization of the smooth conditions eliminates this problem without compromising the physical validity of the results. The flows due to the rigid-wall and smooth conditions are topologically equivalent; differences are entirely quantitative [16,25].

C. Time-periodic forcing protocol

The flow is driven by a systematic repetition of a prescribed forcing protocol. This results in a time-periodic flow of the form

$$\mathbf{u}(\mathbf{x},t+T) = \mathbf{u}(\mathbf{x},t), \tag{2}$$

with $T = nT_{\text{step}}$ the total period time and n the number of forcing steps with fixed duration T_{step}. We use the same time-periodic forcing protocol as employed in [25]. Here each forcing period consists of three consecutive translations of the bottom wall with a stepwise offset angle $\Theta = 2\pi/3$ and stepwise dimensionless displacement D. This yields

$$\theta_{\text{step}} = (k-1)\Theta, \quad D_{\text{step}} = D, \tag{3}$$

as forcing conditions for steps $1 \leqslant k \leqslant 3$. The bottom wall travels in counterclockwise direction along the sides of an equilateral triangle (Fig. 1).

D. Flow composition and perturbation

The stepwise steady boundary conditions cause the flow during the step k to identify with reorientations of the steady flow $\mathbf{u}_s$ induced by the translation of the bottom wall in the positive x direction. Hence, the flow during step k is given by

$$\mathbf{u}(r,\theta,z) = \mathbf{u}_s(r,\theta - k\Theta,z), \tag{4}$$

with $\mathbf{u}_s$ being the base flow. Moreover, the base flow $\mathbf{u}_s$—and thereby the total flow $\mathbf{u}$—can be considered to be a superposition of an unperturbed primary flow $\mathbf{u}_0$ and a weak secondary flow $\mathbf{u}'$, i.e.,

$$\mathbf{u}_s(r,\theta,z) = \mathbf{u}_0(r,\theta,z) + \mathbf{u}'(r,\theta,z), \tag{5}$$

where $\mathbf{u}_0$ coincides with the Stokes limit $\text{Re} = 0$.

The secondary flow $\mathbf{u}'$ can be introduced numerically in two ways. First, by explicitly considering a weak fluid inertia (nonzero $\text{Re} \ll 1$) and a numerical resolution of the full base flow $\mathbf{u}_s$ using the aforementioned spectral flow solver [13,17], the secondary flow can be implicitly defined as

$$\mathbf{u}'(r,\theta,z;\text{Re}) = \mathbf{u}_s - \mathbf{u}_0. \tag{6}$$

Second, $\mathbf{u}'$ can be introduced directly by an additional translation of the top wall at an angle $\theta = \theta_0$ and relative magnitude ε under noninertial conditions. The top-wall translation alone results in a flow field,

$$\mathbf{u}'(r,\theta,z;\varepsilon,\theta_0) = \varepsilon \mathbf{u}_0(r,\theta - \theta_0, -z), \tag{7}$$

and in the linear Stokes limit admits direct superposition upon the unperturbed base flow $\mathbf{u}_0$ following (5).

Parameters (ε,θ_0) are attuned such that $\mathbf{u}'$ according to (6) and (7) are of comparable magnitude for given Re. Thus, the alternative perturbation via the top wall enables the emulation of the role of weak fluid inertia. Note that a similar method, termed *Reynolds-number correction*, is adopted in [28]. However, it must be stressed that both perturbations are physically meaningful. In fact, they trigger essentially similar dynamics in the limit of weak perturbation. This universality in response

is a key to the comparative numerical-experimental analysis below.

E. Tracer motion as stroboscopic map

Tracer motion is governed by the kinematic equation $d\mathbf{X}/dt = \mathbf{u}$, with $\mathbf{X}$ the current position of a tracer released at position $\mathbf{X}_0$. The periodicity (2) of the flow admits an alternative description of the tracer motion by a stroboscopic map,

$$\mathbf{X}_{i+1} = \mathbf{X}_i + \mathbf{m}(\mathbf{X}_i) = \mathbf{X}_i + \mathbf{m}_0(\mathbf{X}_i) + \mathbf{m}'(\mathbf{X}_i). \quad (8)$$

Here $\mathbf{X}_i$ the tracer position after the ith period. The total map $\mathbf{m}$ can, consistent with the flow field, be formally decomposed into a contribution $\mathbf{m}_0$ by the unperturbed flow $\mathbf{u}_0$ and a contribution $\mathbf{m}'$ with relative magnitude,

$$\xi = |\mathbf{m}'|/|\mathbf{m}_0| \ll 1, \quad (9)$$

due the perturbation $\mathbf{u}'$. Note that ξ indicates the perturbation strength for the generic case; it is of $\xi \sim O(\mathrm{Re})$ and $\xi \sim O(\varepsilon)$ for the above perturbations via fluid inertia and the top wall, respectively.

III. EXPERIMENTAL METHODS

Experimental analysis of tracer motion has been carried out by the 3D-PTV using the laboratory setup shown schematically in Fig. 2. This setup is essentially a modified version of that utilized in [25]. It consists of a transparent Perspex cylinder (inner radius, 20 mm; height, 40 mm) that is fixed within a square box. The cylinder-box configuration is held in place by a metal frame (not shown) above a horizontal flat plate. The latter acts as driving bottom wall of the cylinder flow and can perform in-plane translation along any designed path (at a speed set to $u_{\mathrm{wall}} = 2$ mm/s) by a motion-control system (implemented in LABVIEW2007). A minute gap of 0.3 mm is maintained between cylinder and plate to avoid vibrations due to physical contact with the cylinder. (The velocity boundary condition is thus somewhere between the smooth and rigid-wall conditions as per Sec. II B.) Silicon oil (AK 10 000, Wacker GmbH, Germany) has been employed as the working fluid; its kinematic viscosity $\nu = 10^{-2}$ m^2/s and density $\rho = 970$ kg/m^3 ensure laminar flow conditions ($\mathrm{Re} = u_{\mathrm{wall}}R/\nu \leqslant 2 \times 10^{-3}$). The cylinder is submerged in a shallow fluid layer of about 5 mm on the flat plate (contained by sidewalls) in order to prevent fluid leakage from the cylinder and entrainment of air during the wall translation. The flow domain is filled with the working fluid via the removable top lid (Fig. 2).

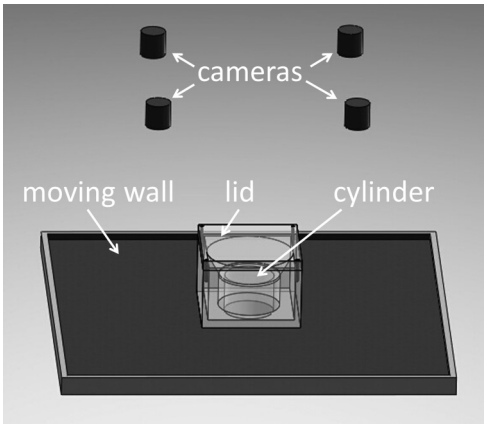

FIG. 2. Schematic of the laboratory setup for particle tracking by 3D-PTV.

The fluid is seeded by polystyrene tracer particles (diameter 20 μm) that are tracked by four CCD cameras (specifications are in [25]) facing the cylinder interior through its top wall (Fig. 2). Data processing of the particle imagery for determination of velocity vectors and trajectories is performed with the 3D-PTV algorithm developed at Eidgenössische Technische Hochschule, Zürich, Switzerland [29,30]. This algorithm incorporates optical refraction by said top wall. Hence, there is no need for further suppression or compensation of effects by refraction. Seeding particles are about an order of magnitude smaller than those utilized in [25]; given the same working fluid, this results in a favorable particle dynamics for reliable tracking. Cameras and a motion-control system are synchronized by the same LABVIEW algorithm.

The experiments were conducted at bottom-wall velocity $u_{\mathrm{wall}} = 2$ mm/s and stepwise displacement $D_{\mathrm{wall}} = 80$ mm, resulting in a nondimensional wall displacement $D = 4$. This gives a duration of 40 and 120 s per step and period, respectively, enabling tracking of 30 periods per hour. Recording at a frame rate of 1 Hz yields $4 \times 120 = 480$ images per period of about 2 MB each (nearly 1 GB in total per period). Measurement sessions spanned up to 1200 periods (40 h) and produced up to 576 000 images (around 1.2 TB in data). Storage and (in particular) transfer capacity of the data-acquisition system determined the experimental limits.

IV. LAGRANGIAN FLOW STRUCTURE

A. Periodic lines of the unperturbed flow

The topology of the tracer trajectories in the 3D cylinder flow has been extensively examined before [13–17]. Two features important in the current context are confinement of tracers released in the base flow $\mathbf{u}_s$ to closed streamlines symmetric about the planes $x = 0$ and $y = 0$ [Fig. 3(a)] and, intimately related to that, their restriction to spheroidal invariant surfaces in the corresponding unperturbed time-periodic flow [Fig. 3(b)]. These invariant surfaces are, in fact, level sets of an axisymmetric constant of motion $F_s(\mathbf{x})$, i.e., $F_s(\mathbf{X}_i) = F_s(\mathbf{X}_0)$, which is invariant under map (8) for vanishing $\mathbf{m}'$ [14].

Relevant entities within the invariant surfaces are periodic points, i.e., tracers that systematically return to their initial position after p periods: $\mathbf{X}_{i+p} = \mathbf{X}_i$. Period-$p$ *points* on adjacent invariant surfaces merge into period-p *lines* in the 3D unperturbed flow [15,16]. Their properties are determined by the spectrum $\boldsymbol{\lambda} = (\lambda_1, \lambda_2, \lambda_3) = \mathrm{eig}(\mathbf{F})$ of the deformation tensor

$$\mathbf{F} = \partial \mathbf{X}_p/\partial \mathbf{X}_0 = \mathbf{I} + \partial \mathbf{m}/\partial \mathbf{X}_0, \quad (10)$$

associated with the individual periodic points [9]. Points on periodic lines invariably possess one unit eigenvalue, say $\lambda_1 = 1$, and fall into one of two categories: first, elliptic

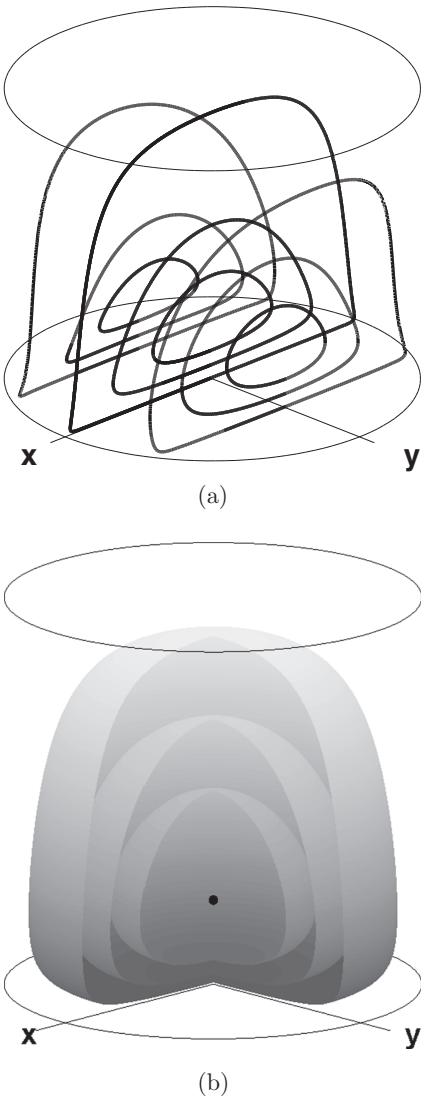

FIG. 3. Fundamental properties of the unperturbed flow. (a) Closed streamlines (symmetric about plans $x = 0$ and $y = 0$) of base flow $\mathbf{u}_s$; (b) invariant spheroids of the time-periodic flow in the noninertial limit $\mathrm{Re} = 0$. Simulation using rigid-wall boundary conditions. (Reproduced from [25].)

points ($\lambda_2 = \lambda_3^* = e^{i\omega}$) defining the centers of continuous families of closed orbits in the stroboscopic map (8) ("elliptic islands") within invariant surfaces; second, hyperbolic points ($\lambda_2 = \lambda_3^{-1} = \lambda$ defining the centers of chaotic regions within invariant surfaces [15]). (Here $i = \sqrt{-1}$ and the symbol "$*$" denotes complex conjugate.) These periodic lines play a key role in the response of the system to perturbations, where distinction between the two types becomes significant.

It is important that, though systematically recurring to the same position, the actual continuous path of a tracer on a periodic orbit generically is quite extensive. Typical tracer paths between two visits to period-1 and period-2 points are shown in Figs. 4 and 5, respectively, demonstrating substantial excursions throughout the domain. (See, e.g., [14] for identification algorithms for periodic points.) Therefore, though the response to perturbation will be studied primarily

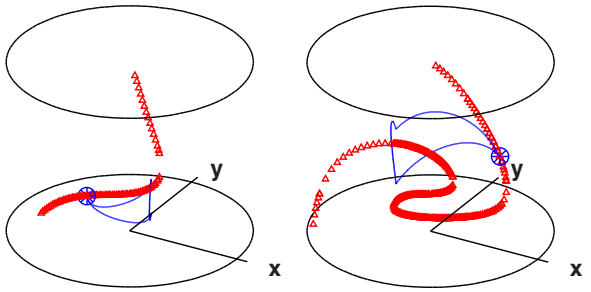

FIG. 4. (Color online) Continuous tracer paths (blue solid line) corresponding with a period-1 point (blue circle) on the period-1 line (red triangles). (a) $D = 4$; (b) $D = 14$. Simulations of the unperturbed flow using smooth boundary conditions.

in terms of stroboscopic map (8), continuous tracking of tracers nonetheless remains necessary for exposing the dynamics. This has consequences, in particular, for experimental analyses, since handling of the corresponding data volumes constitutes the principal limit on the measurement capabilities (Sec. III). Periodwise instead of continuous data acquisition (if possible) would enlarge the experimental range by about two orders of magnitude.

B. Universality in response to perturbation

Perturbation of the system by weak fluid inertia, inducing nonzero secondary flow $\mathbf{u}'$, (6), destroys the invariant surfaces and leads to significantly different tracer dynamics [13,16,17]. Tracers exhibit distinct behavior depending on their proximity to elliptic segments of periodic lines. Tracers "far away" from such periodic lines oscillate about the original invariant surface and, in the long term, average out the effect of the secondary motion. As a result, tracers remain entrapped in shells ("adiabatic shells") of thickness $O(\sqrt{\xi})$, with ξ defined in (9), centered on its original invariant surface [16]. The corresponding constant of motion $F_s(\mathbf{x})$ becomes an *adiabatic invariant* of the perturbed flow. On the other hand, tracers "near" periodic lines may escape from their original shell and be transported to another shell through a connecting tube [emerging in stroboscopic map (8)] centered on the elliptic segment of a given periodic line. This is demonstrated in Fig. 6(a) by way of the stroboscopic map of a single tracer

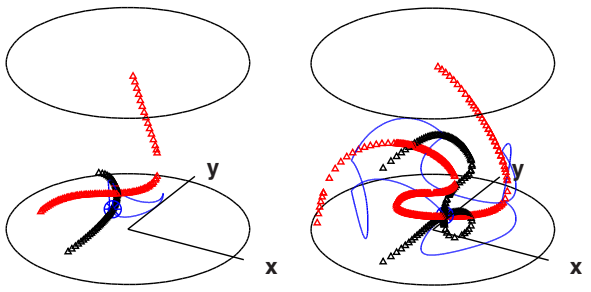

FIG. 5. (Color online) Continuous tracer paths (blue solid line) corresponding with a period-2 point (blue circle) on the period-2 line (black/dark triangles). (a) $D = 4$; (b) $D = 14$. Period-1 lines (red/gray triangles) are included for reference. Simulations of the unperturbed flow using smooth boundary conditions.

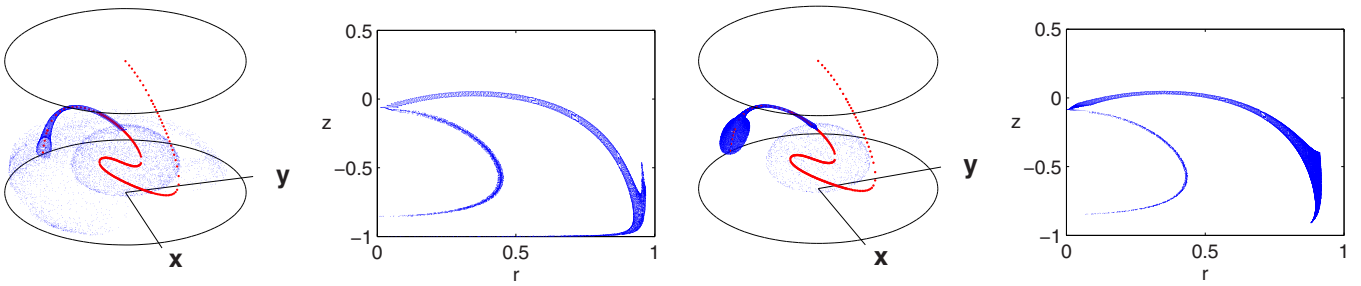

FIG. 6. (Color online) Formation of tubes on the period-1 line (red/large markers) connecting adiabatic surfaces under weak perturbation ($D = 14$). (a) Fluid inertia (Re $= 0.005$); (b) top-wall motion ($\varepsilon = 0.0005, \theta_0 = \pi/6$). Visualization by the 3D perspective and $r - z$ projection of the stroboscopic map of a single tracer (blue/small markers). Simulations using smooth boundary conditions.

released near the tube on the inner shell and tracked both forward and backward in time. Note that this behavior may happen for periodic lines of basically any periodicity p [16,17].

The alternative perturbation via the top wall, inducing nonzero secondary flow $\mathbf{u}'$ of comparable magnitude [see (7)] triggers essentially the same behavior. This is demonstrated in Fig. 6(b) by a tracer released at the same position as that in Fig. 6(a). The structures are in close agreement in both cases. Notable differences between both kinds of perturbation occur only near the cylinder wall, where the secondary flow of the wall-induced perturbation becomes much smaller than its inertia-induced counterpart. Here motion in the former case slows down considerably, causing tracers to remain confined for prolonged periods of time before entering the outer shell. This is reflected by the relatively higher tracer density in this area in Fig. 6(b).

The above findings illustrate that the system responds to weak perturbations in a universal way that is *dependent* on the strength of the perturbation [quantified by ξ according to (9)] yet is *independent* on its nature. This universality is crucial to the numerical-experimental analysis below by admitting comparison of perturbed dynamics without the need to exactly replicate the perturbation. Numerical simulations may employ the perturbations following Sec. II D; laboratory experiments can rely on experimental imperfections as natural perturbation.

The above universality in response to weak perturbations confirms the analytical results following [19], where it was shown that the ensuing global behavior in flows with invariant surfaces containing periodic points (which includes the present spheroidal surfaces) is independent of the exact form of the perturbation. The only condition is that it has a finite component normal to the adiabatic surface at the periodic points, which is, in accordance with general theory, treated in [31,32].

C. Structure of the tubes

Tracers nearing the vicinity of elliptic (segments of) periodic lines, instead of remaining within an adiabatic shell, gradually leave that shell via tubes centered on these lines as demonstrated in Fig. 6. The formation of such tubes is due to resonances of the secondary motion in a stroboscopic map (8). More specifically, tubes form on the 1D manifolds of isolated periodic points in map (8) that emanate from breakup of periodic lines. This mechanism has been investigated in detail in [18] for a comparable 3D time-periodic flow and is suspected to also occur here (conclusive establishment is outstanding).

Each periodic point on an elliptic (segment of a) periodic line defines the center of a continuous family of closed orbits on an invariant surface (i.e., the elliptic islands according to Sec. IV A). Perturbation causes the matching islands on neighboring shells to merge into concentric tubes that provide a pathway for tracer transport. (Tracers always travel from an inner shell to an outer shell in the cases considered here.) On each shell, the outmost closed trajectory of the base flow around the elliptic point of the periodic line defines the *entrance zone* into the tube. The area of the entrance zone is a function of the perturbation strength ε and the value of the adiabatic invariant $F_s(\mathbf{x})$. Tracers randomly moving in an adiabatic shell may at some point enter the entrance zone and, upon doing so, start propagating along the tube instead of continuing their excursion in the shell. This entrapment is very similar to the phenomenon of "capture into resonance" studied in [21]. When a tracer switches from the motion on an adiabatic shell to the motion in a tube, it performs a fast switch between two drastically different adiabatic invariants. The motion on shells namely has its own adiabatic invariant, and the motion along the tube has a completely different adiabatic invariant. This entrapment is very similar to the phenomenon of "capture into resonance" first described in [33] and first studied in applications to fluid flows (or volume-preserving systems) in [21].

Individual tracer entering a tube outlines its extent by describing a tight spiral that consequently intersects neighboring shells next (Fig. 7). Each coil of the spiral lies approximately on the shell that the tracer is intersecting at a given moment. Thus, multiple tracers describe a nested family of concentric tubes centered on the periodic line, as demonstrated in Figs. 8(a) and 8(b). At certain moments, different for different tracers and defined by the conservation of the tube adiabatic invariant (introduced below), tracers leave the tubes and emerge on new shells.

D. Adiabatic invariant for the tubes

The tracer motion through the tube consists of three parts: capture into the tube, transport through the tube, and release from the tube. In this section, we aim at seeking an adiabatic invariant, complementary to the adiabatic invariant $F_s(\mathbf{x})$ of

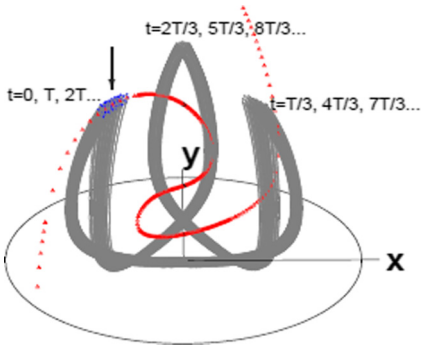

FIG. 7. (Color online) Continuous tracer path (gray) of the single tracer outlining the period-1 tube (blue; indicated by arrow) on the period-1 line (red triangles) ($D = 14$). Perturbation by fluid inertia (Re $= 0.005$). Simulations using smooth boundary conditions.

the adiabatic shells (Sec. IV B), that is embedded in the tube dynamics.

Consider a point A on a given tube. There exists a closed curve of unperturbed stroboscopic points [$\mathbf{m}' = \mathbf{0}$ in terms of map (8)], Γ_A, passing through A. This curve lies on the shell that the tube is intersecting and encloses the local cross-sectional area of the shell, S_A. Thus, $\Gamma_A = \partial S_A$. At every point $\mathbf{X}_i \in S_A$, we can introduce a velocity vector $\mathbf{V}_i = (\mathbf{X}_{i+1} - \mathbf{X}_i)/T$ generated by map $\mathbf{m}(\mathbf{X})$. We define the flux of perturbation as

$$\Psi = \frac{1}{\xi}\int_{S_A} \mathbf{V}_i \cdot \mathbf{n}\, d\sigma, \tag{11}$$

where $\mathbf{n}$ and $d\sigma$ are the unit normal and area element of S_A, respectively, and ξ corresponds with the relative perturbation strength (9). The positive direction of $\mathbf{n}$ is taken to be the direction of the angular velocity of the unperturbed motion along Γ_A.

The component of $\mathbf{V}_i$ that corresponds to $\mathbf{m}_0$ does not contribute to the flux, since its direction is in the same plane as S_A. Thus, (11) reduces to

$$\Psi = \frac{1}{\xi}\int_{S_A} \mathbf{V}'_i \cdot \mathbf{n}\, d\sigma, \tag{12}$$

where $\mathbf{V}'_i$ is the velocity component induced by the perturbation $\mathbf{m}'$. The definition of Ψ is a generalization of the definition of an adiabatic invariant introduced in [10,23] for volume-preserving flows to stroboscopic maps. Thus, we can expect Ψ to be conserved for a tracer traveling along a tube, in other words, to define the sought-after adiabatic invariant: $\Psi(\mathbf{X}_i) = \Psi(\mathbf{X}_0)$ for tracer positions $\mathbf{X}_i$ inside the family of tubes.

Function Ψ is evaluated for the three concentric tubes shown in Fig. 8(a). To this end one point on each tube was selected as an initial condition. It is somewhat complicated to evaluate $\mathbf{V}'_i$ at every point inside S_A. However, one can see that the cross-sectional area is relatively small for most part of the tube. This provides the possibility of applying the averaged value of $\mathbf{V}'_i$ on a given S_A for the computation of Ψ. The tracer is swirling around the period-1 line to form a tube. So $\mathbf{V}'_i$ can be approximated by the velocity of the period-1 fixed point in S_A. Moreover, $\mathbf{V}'_i = \mathbf{0}$ in the absence of perturbation, since $\mathbf{m}_0$ is

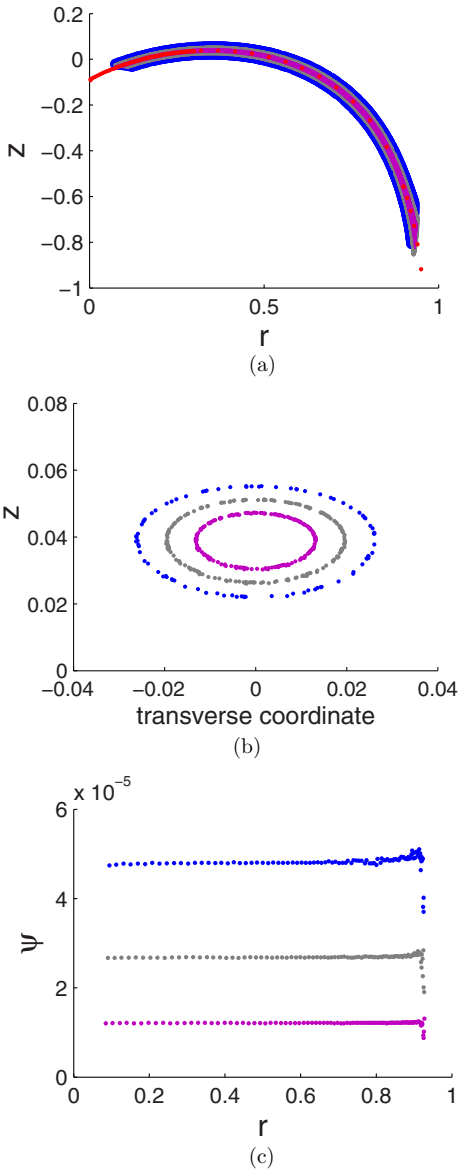

FIG. 8. (Color online) Adiabatic invariance in period-1 tubes demonstrated for three concentric period-1 tubes (purple/gray/blue; inner/middle/outer) induced by fluid inertia (Re $= 0.005$). (a) $r - z$ projection; (b) cross section perpendicular to symmetry plane $\theta = \pi/6$; (c) adiabatic invariant Ψ following (12) along the tubes (purple/gray/blue: lower/middle/upper). Simulations for $D = 14$ using smooth boundary conditions.

not contributing and perturbation $\mathbf{m}' = \mathbf{0}$, which is consistent with the property of a period-1 point (i.e., fixed point in the map). Thus, we arrive at

$$\Psi \approx \frac{1}{\xi} S_A(\mathbf{V}'_i \cdot \mathbf{n}). \tag{13}$$

The conservation of Ψ defines the input-output function for the transport through the tubes. Suppose a given tracer entered the tube from a certain shell. Then the area of S_A at that moment is equal to the area of the entrance zone. Initially, as the tracer moves inside the tubes, the area of the entrance zone on the shells that the tracer is passing by increases. Thus, the tracer

stays inside the tubes. However, after a while, the dynamics changes: As the tracer comes closer to the side of the cylinder, the values of $\mathbf{V}_i'$ decrease. Therefore, for Ψ to be conserved, the value of S_A must increase. At a certain shell the value of S_A for the tracer in question reaches the value of the entrance zone on that shell. As a result, the tracer cannot "fit" in the tube anymore and exits the tube to that new shell. This mechanism can be described as last-in–first-out: The deeper was the shell where a tracer got into the tube, the longer it stays in the tube, thus getting out closer to the side of the cylinder.

Figure 8(c) gives the function Ψ obtained by the above approximation throughout each of the concentric tubes. The function values clearly retain at a distinct (approximately) constant level in the entire tube area, demonstrating that Ψ indeed defines an adiabatic invariant. The smaller is the value of Ψ, the closer the tube is to the period-1 line. Moreover, Ψ is best conserved in the region where the cross-sectional area of the tube is relatively small. Hence, shown approximations of Ψ are relatively more accurate in the smaller tubes (purple/inner, gray/middle) compared to the larger tube (blue/outer). The numerical approximation becomes inaccurate as the tracer approaches the tube exits ($r > 0.85$). This is caused by (i) the rapid increase in cross-sectional area and (ii) the existence of a hyperbolic segment of the period-1 line nearby, which renders evaluation of $\mathbf{V}_i'$ imprecise. A rapid change in Ψ as the tracers approaching the escape zone is shown in Fig. 8(c), which indicates that the motion of the tracer on shell is characterized by a different adiabatic invariant, $F_s(\mathbf{x})$, instead of Ψ (Sec. IV B). The presence of an adiabatic invariant Ψ for the tubes has important implications. First, it proves that the tubes indeed constitute distinct and complete coherent structures (in the sense of individually belonging to one smooth and regular level set of Ψ). Second, it deterministically and uniquely connects a given inner shell with a given outer shell via a distinct tube. These findings, in turn, imply that the union of tubes and shells (denoted "adiabatic structures" in [16]) also define distinct coherent structures.

V. EXPERIMENTAL INVESTIGATION

A. Validation of the base flow

The base flow $\mathbf{u}_s$ is the elementary "building block" of the time-periodic flow fields and its validation is important to asses the overall quality of the experimental data. This concentrates primarily on a qualitative matching of fundamental properties in the Stokes limit rather than on one-to-one quantitative agreement with numerical simulations. Minor deviations in boundary conditions at the driving bottom wall essentially preclude this (Secs. II B and III). However, similar to [25], this is inconsequential for the fundamental dynamics. Relevant properties are (i) closed streamlines; (ii) symmetric streamlines about planes $x = 0$ and $y = 0$; (iii) coincidence of the stepwise flow with reorientations of the base flow [25]. To this end, velocity fields and corresponding trajectories are measured separately for each of the three forcing steps. Moreover, the flow forcing is performed with the translation of the bottom wall in both forward and reversed directions. Thus-obtained six separate data sets were *a posteriori* combined into one field, where each set was reoriented such that the forcing direction coincided with that of the base flow. Hence, the combined field should match the base flow and possess the fundamental properties discussed above within an acceptable tolerance. Analysis similar to [25] proved the experimental data to be of sufficient quality for the present study.

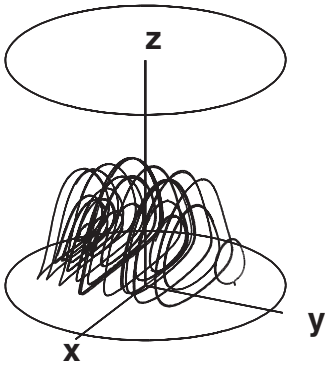

FIG. 9. Streamlines of the base flow obtained from laboratory experiments by particle tracking using 3D-PTV.

Figure 9 presents a number of typical streamlines taken from the six (reoriented) data sets. This visually demonstrates that together they indeed constitute a coherent family of streamlines that are closed and symmetric about planes $x, y = 0$ within acceptable error margins. Note the close (qualitative) agreement with the streamlines obtained from the analytical velocity field shown in Fig. 3(a).

B. Period-1 lines

Experimental data for time-periodic flows are obtained from long-term experiments (1200 periods) with dimensionless displacement $D = 4$. Two data sets are generated: one with periodwise step sequence $k = \{1,2,3\}$; one with reversed step sequence $k = \{3,2,1\}$ and reversed stepwise forcing direction. Former and latter data sets define time-reversal counterparts in the Stokes limit. The fundamental entities of interest in these flows, i.e., periodic lines, must match for forward and time-reversed flows [13]. Verification of this property enables further assessment of the data quality.

The present three-step flow accommodates period-1 lines in the symmetry plane $\theta = \pi/6$, the presence of which has been demonstrated experimentally in [25]. However, through an analysis analogous to [34], additional period-1 lines, emerging in pairs symmetric about the $\theta = \pi/6$ plane, can be identified. Figure 10 shows simulated period-1 lines (curves described by red markers) in comparison to the combined experimental results (blue/scattered markers). The latter clearly outline well-defined entities and, in that sense, validate the presumed time reversibility of the flow. Moreover, the experimental period-1 lines both within and outside the symmetry plane are in a close agreement with their simulated counterparts. (Note that the experimental data only partially reveal the pair of period-1 lines outside the symmetry plane.) Differences between numerical and experimental lines are mainly quantitative and must be attributed to aforementioned deviations in the boundary conditions. Exposure of period-1 lines outside the symmetry plane further consolidates the first experimental evidence of their existence provided in [25].

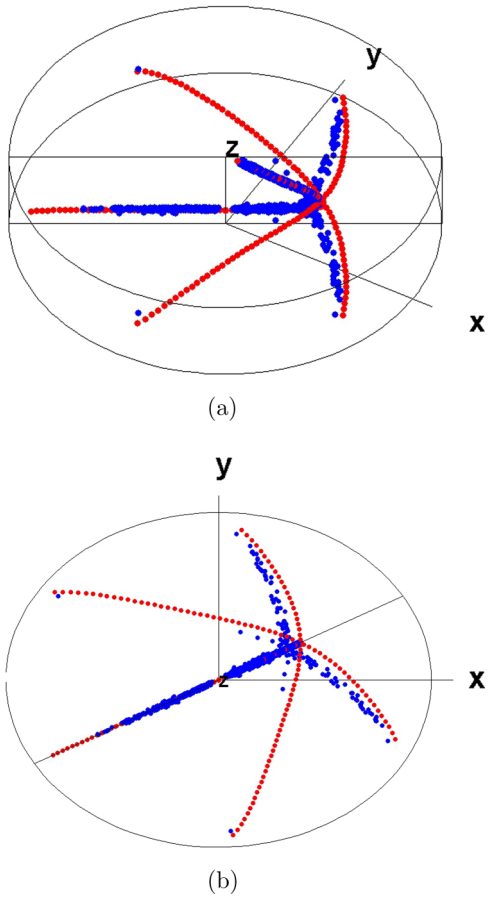

FIG. 10. (Color online) Period-1 lines obtained by 3D-PTV (blue/scattered markers) versus numerical simulations rigid-wall boundary condition (curves described by red markers) for $D = 4$. (a) 3D perspective view; (b) top view. The black frame in panel (a) outlines symmetry plane $\theta = \pi/6$.

C. Period-1 tubes

The numerical study in Sec. IV revealed a significant impact of even very weak perturbations on the long-term dynamics of the system by triggering the formation of tubes connecting adiabatic shells. Moreover, this impact transpired as universal in that it depended only on the strength of the perturbation yet *not* on its nature. Both weak fluid inertia and minute disturbances of the flow forcing affected the dynamics in the same way. This strongly suggests that small imperfections in experimental conditions (e.g., geometry, nonpassive tracer particles) will have a similar impact on the long-term behavior. Hence, such imperfections can be exploited as a natural perturbation in laboratory experiments.

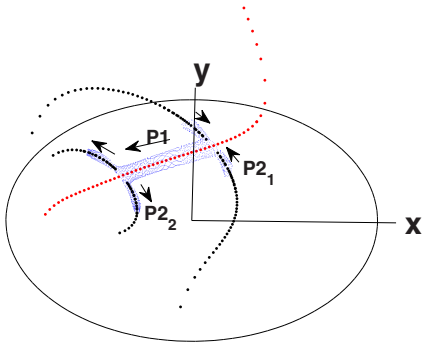

FIG. 12. (Color online) Tube bifurcation at intersections of period-1 (red/dark gray) and period-2 (black) lines demonstrated by the stroboscopic map (blue/light gray) of a single tracer for $D = 4$. Labels indicate period-1 ($\mathcal{P}_1$) and period-2 ($\mathcal{P}2_{1,2}$) tubes; arrows indicate direction of motion. Numerical simulations using top-wall perturbation ($\varepsilon = 0.0005, \theta_0 = \pi/6$) and rigid-wall boundary conditions.

Figure 11(a) presents a long-term stroboscopic dynamics of a single tracer (tube described by blue markers) tracked by the 3D-PTV in relation to the experimental period-1 line (curve described by red markers). A spiraling orbit outlines the portion of a tube centered on the period-1 line. Comparison with the numerical simulations shown in Fig. 11(b), obtained using the rigid-wall boundary conditions and the top-wall disturbance as a weak perturbation ($\varepsilon = 0.0005$ and $\theta_0 = \pi/6$), reveals an excellent agreement. Experimentally measured and simulated structures are very similar in location and extent. This experimentally validates two fundamental properties: (i) The tube formation is induced by weak perturbations; (ii) the response to weak perturbations is universal.

D. Tube bifurcation

Instead of connecting with adiabatic shells, tubes may undergo bifurcations in higher-order tubes [13,16]. In fact,

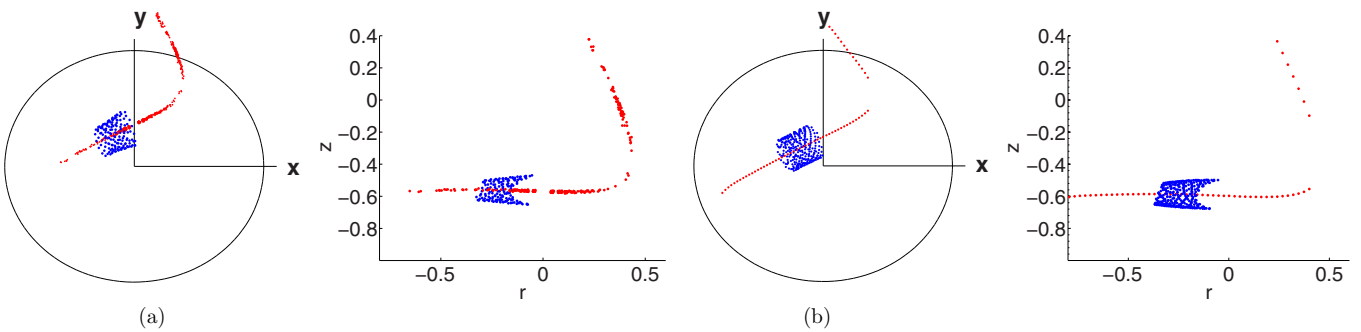

FIG. 11. (Color online) Formation of a period-1 tube on the period-1 line (curve described by red markers) demonstrated by the stroboscopic map of a single tracer (tube described by blue markers) for $D = 4$. (a) Experiments using 3D-PTV; (b) numerical simulations using top-wall perturbation ($\varepsilon = 0.0005$ and $\theta_0 = \pi/6$) and rigid-wall boundary conditions.

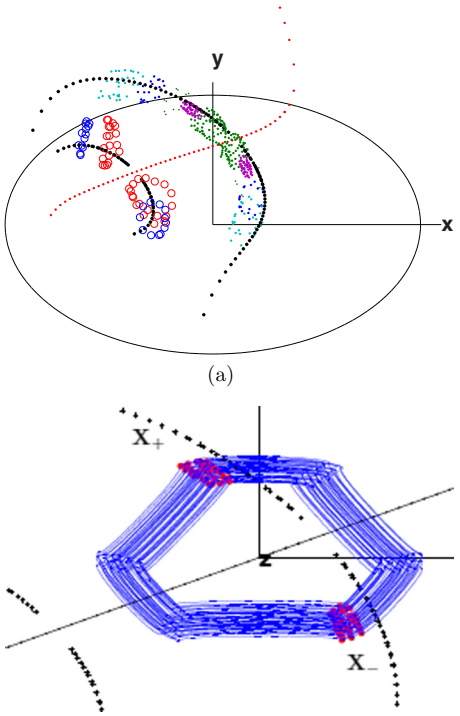

FIG. 13. (Color online) Experimental evidence for period-2 behavior consistent with the formation of period-2 tubes for $D = 4$. (a) Maps of individual tracers (distinguished by color/grayscale and marker size) centered on simulated period-2 lines (curves described by black markers); (b) periodwise alternation of a single tracer between positions $\mathbf{X}_+ = \{\mathbf{X}_0, \mathbf{X}_2, \dots\}$ and $\mathbf{X}_- = \{\mathbf{X}_1, \mathbf{X}_3, \dots\}$ (large markers) on either side of symmetry plane $\theta = \pi/6$. The curve bisecting period-2 lines indicates period-1 line; solid lines in panel (b) indicate continuous tracer paths.

the period-1 tube partially outlined in Fig. 11 exhibits such a behavior at both its ends upon reaching two intersections of the period-1 line with two period-2 lines. This is demonstrated in Fig. 12 by numerical simulations. Two elliptic period-2 lines (black) are symmetric about the symmetry plane ($\theta = \pi/6$), and both intersect the period-1 line (red/dark gray). The period-1 tube ($\mathcal{P}_1$) confluences with two period-2 tubes $\mathcal{P}2_1$ and $\mathcal{P}2_2$. Tracers migrate in one direction, indicated by the arrows, along the tube structure: advection along the period-2 tube $\mathcal{P}2_1$ towards the first intersection; switch to the period-1 tube $\mathcal{P}_1$; advection along $\mathcal{P}_1$ towards the second intersection; switch to the period-2 tube $\mathcal{P}2_2$; advection along $\mathcal{P}2_2$. The entrance and exit of the period-2 tubes $\mathcal{P}2_1$ and $\mathcal{P}2_2$, respectively, connect with adiabatic shells (not shown). Hence, this tube arrangement, though of a more intricate structure, connects two adiabatic shells in essentially the same way as observed for period-1 tubes.

Experimental investigation of the tube bifurcation is extremely challenging due to the slow nature of this phenomenon. Traveling through the entire tube structure takes thousands of periods while the experimental data cover only 1200 periods. Hence, at present, only experimental validation via circumstantial evidence is feasible. We concentrate on two aspects: (i) the experimental demonstration of period-2 behavior consistent with formation of the period-2 tubes and (ii) the experimental demonstration of tube bifurcation at the intersections of period-1 and period-2 lines.

Figure 13(a) shows the stroboscopic map of several experimental tracer particles (labeled by color/grayscale and marker size) in the vicinity of the simulated period-2 lines (curves described by black markers). Each tracer alternates between either side of the symmetry plane (signifying period-2 motion) and thus gradually outlines a pair of spiraling orbits centered on one of the period-2 lines. This periodwise alternation between positions $\mathbf{X}_+ = \{\mathbf{X}_0, \mathbf{X}_2, \dots\}$ and $\mathbf{X}_- = \{\mathbf{X}_1, \mathbf{X}_3, \dots\}$ in the stroboscopic map is shown in detail in Fig. 13(b) for one particular tracer (compare the pattern described by the corresponding continuous path with that of the period-1 trajectories in Fig. 7). This reveals a close correlation between the simulated period-2 behavior and observed tracer dynamics in the experiments, thus establishing at least a fundamental consistency with the formation of period-2 tubes.

Figure 14(a) illustrates the simulated tracer dynamics (tubelike structures described by blue markers) at the confluence of the period-1 line (curve described by red markers) and one of the period-2 lines (not shown). The tracer progresses from right to left and, instead of continuously spiraling around the period-1 line, thus outlining a tube, develops a "hole" in the tube at the location of the intersection between period-1 and period-2 lines, before resuming its spiraling motion at a substantially larger radius. Period-2 tube $\mathcal{P}2_1$ of the structure shown in Fig. 12 (also outlined by a single tracer) penetrates

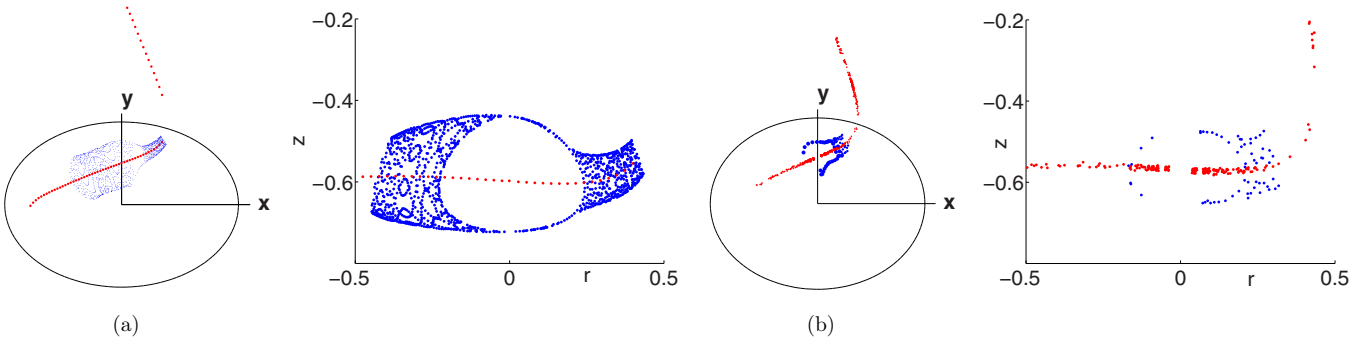

FIG. 14. (Color online) Tracer dynamics near the tube bifurcation on the period-1 line (curve described by red markers) demonstrated by the stroboscopic map (tubelike structures described by blue markers) of a single tracer for $D = 4$. (a) Numerical simulations using top-wall perturbation and rigid-wall boundary conditions; (b) experiments using 3D-PTV. Shown are 3D perspective and $r - z$ projection.

the above "hole" and continues towards the left as period-1 tube $\mathcal{P}_1$, where the latter is enclosed by the left segment of the period-1 tube in Fig. 12. This signifies highly complicated (and very peculiar) dynamics in this area. Figure 14(b) shows the stroboscopic map of an experimental tracer in this area. Its behavior that is entirely consistent with the simulations (seen the most clearly in the $r-z$ projections) in that the tracer, while moving leftwards, also starts with demarcating a tube segment, subsequently outlines the "hole area" and then returns to a spiraling motion about the period-1 line. Note that only first signs of the latter stage in the experimental tracer propagation could be made visible due to the limited data available in this particular region. This nonetheless provides a further important (circumstantial) experimental evidence of the tube bifurcation at the intersections of period-1 and period-2 lines.

VI. CONCLUSIONS

In the present study we investigated the impact of weak perturbations on the Lagrangian flow structure of 3D unsteady deterministic flows. We adopted a 3D time-periodic laminar flow inside a lid-driven cylinder as representative experimentally realizable system. Theoretical-numerical analyses addressed fundamental issues of the response of the 3D time-periodic Stokes flow driven solely by the bottom wall to weak perturbations. Laboratory experiments performed using the 3D-PTV have been performed for experimental analysis and validation of key aspects of the observed dynamics.

The Lagrangian flow structure of the unperturbed time-periodic flow consists of a global family of nested spheroidal invariant surfaces. Perturbation of this state has been induced in two separate ways: (i) weak fluid inertia and (ii) disturbance of the flow forcing by slight motion of the top wall. The parameters of the latter were attuned to attain comparable perturbation strengths. This yielded essentially identical responses in that both perturbations resulted in transition to the same state, comprising intricate coherent structures, formed by merger of adiabatic shells emanating from (remnants of) spheroids and tubes, embedded in chaos. This conclusively demonstrated the universal nature of the role of weak perturbations in the Lagrangian dynamics of flows with invariant surfaces containing periodic points.

Furthermore, the existence of a separate adiabatic invariant for the tubes has been demonstrated, which has important implications. First, it proves that the tubes indeed constitute distinct coherent structures. Second, it deterministically connects a unique pair of adiabatic shells via a distinct tube. This, in turn, implies that the coherent structures thus formed also define distinct entities that admit representation by an adiabatic invariant.

Experimental investigation strengthened earlier observations that periodic lines indeed emerge in actual physical systems. Here existence of periodic lines both within and symmetrically arranged about a designated plane has been demonstrated. Moreover, experimental evidence for the formation of tubes on periodic lines has been found. Substantial portions of period-1 tubes have been directly isolated from 3D-PTV data; circumstantial evidence for period-2 tubes and tube bifurcations has been found. These findings, besides the phenomena themselves, experimentally validated the universality of the response to weak perturbations. The laboratory experiments namely relied entirely on small imperfections as a natural perturbation. This, in fact, exposed the weakly perturbed state as the true "unperturbed state" in realistic systems.

Ongoing and future efforts concentrate on several topics. Essential is continued experimental analysis and validation of long-term dynamics so as to further support theoretical and numerical results. Here an important challenge is further development of the 3D-PTV algorithms in order to enable longer tracking of individual tracer particles. The longest tracks in the data sets employed in this study (spanning 1200 periods), e.g., covered a few hundred periods. Extending the track length of a substantial amount of tracers to the total duration of the experiment would tremendously enhance the experimental analysis without the need for longer experiments (a major challenge in its own right). A further subject of great interest is the universality of the response to perturbation. Here a central question is whether similar behavior can be induced by, e.g., nonpassive particles (lift, buoyancy) or thermal effects (fluid buoyancy).

ACKNOWLEDGMENTS

We sincerely acknowledge A. P. C. Holten and F. M. R. van Uittert of the Fluid Dynamics Laboratory for their great technical support. F.W. and D.V. were partially supported by the NSF (Award No. CMMI-1362782). D.V. was also supported in part by the RFBR (Award No. 13-01-00251).

[1] H. Tennekes and J. L. Lumley, *A First Course in Turbulence* (MIT Press, Cambridge, MA, 1992).
[2] P. E. van Keken, E. H. Hauri, and C. J. Ballentine, Annu. Rev. Earth Planet Sci. **30**, 493 (2002).
[3] S. Wiggins, Annu. Rev. Fluid. Mech. **37**, 295 (2005).
[4] N. Harnby, M. F. Edwards, and A. W. Nienow, *Mixing in the Process Industries* (Butterworth-Heinemann, Oxford, UK, 1997).
[5] R. Weinekötter, Trends Food Sci. Tech. **20**, S48 (2009).
[6] H. A. Stone, A. D. Stroock, and A. Ajdari, Annu. Rev. Fluid Mech. **36**, 381 (2004).
[7] P. L. Mills, D. J. Quiram, and J. F. Ryley, Chem. Eng. Sci. **62**, 6992 (2007).
[8] B. Weigl, G. Domingo, P. Labarre, and J. Gerlach, Lab Chip **8**, 1999 (2008).
[9] J. M. Ottino, *The Kinematics of Mixing: Stretching, Chaos and Transport* (Cambridge University Press, Cambridge, UK, 1989).
[10] A. I. Neishtadt, D. L. Vainchtein, and A. A. Vasiliev, Physica D **111**, 227 (1998).
[11] H. Aref, Phys. Fluids **14**, 1315 (2002).
[12] S. Wiggins and J. M. Ottino, Philos. Trans. R. Soc., A **362**, 937 (2004).

[13] Z. Pouransari, M. F. M. Speetjens, and H. J. H. Clercx, J. Fluid Mech. **654**, 5 (2010).
[14] V. S. Malyuga, V. V. Meleshko, M. F. M. Speetjens, H. J. H. Clercx, and G. J. F. van Heijst, Proc. R. Soc. London, Ser. A **458**, 1867 (2002).
[15] M. F. M. Speetjens, H. J. H. Clercx, and G. J. F. van Heijst, J. Fluid Mech. **514**, 77 (2004).
[16] M. F. M. Speetjens, H. J. H. Clercx, and G. J. F. van Heijst, Phys. Fluids **18**, 083603 (2006).
[17] M. F. M. Speetjens, H. J. H. Clercx, and G. J. F. van Heijst, Chaos **16**, 043104 (2006).
[18] N. R. Moharana, M. F. M. Speetjens, R. R. Trieling, and H. J. H. Clercx, Phys. Fluids **25**, 093602 (2013).
[19] I. Mezic, Physica D **154**, 51 (2001).
[20] T. H. Solomon and I. Mezic, Nature (London) **425**, 376 (2003).
[21] D. L. Vainchtein, A. I. Neishtadt, and I. Mezic, Chaos **16**, 043123 (2006)
[22] D. L. Vainchtein, J. Widloski, and R. O. Grigoriev, Phys. Rev. E **78**, 026302 (2008).
[23] D. L. Vainchtein, A. A. Vasiliev, and A. I. Neishtadt, Chaos **6**, 67 (1996).
[24] A. Neishtadt, D. Vainchtein, and A. Vasiliev, in *IUTAM Symposium on Hamiltonian Dynamics, Vortex Structures, Turbulence*, edited by A. V. Borisov, V. V. Kozlov, I. S. Mamaev, and M. A. Sokolovskiy, IUTAM Bookseries Vol. 6 (Springer, Netherlands, 2008), pp. 89–107.
[25] J. Znaien, M. F. M. Speetjens, R. R. Trieling, and H. J. H. Clercx, Phys. Rev. E **85**, 066320 (2012).
[26] P. N. Shankar, J. Fluid Mech. **342**, 97 (1997).
[27] M. F. M. Speetjens and H. J. H. Clercx, Int. J. Comput. Fluid Dyn. **19**, 191 (2005).
[28] K. Bajer and H. K. Moffatt, in *Topological Aspects of the Dynamics of Fluid and Plasmas*, edited by H. K. Moffatt, G. M. Zaslavsky, P. Comte, and M. Tabor, NATO ASI Series Vol. 218 (Springer, Berlin, 1992), pp. 517–534.
[29] J. Willneff, Ph.D. Dissertation, Technische Wissenschaften, ETH Zurich, 2003.
[30] B. Luethi, A. Tsinober, and W. Kinzelbach, J. Fluid Mech. **528**, 87 (2005).
[31] V. I. Arnold, V. V. Kozlov, and A. I. Neishtadt, in *Encyclopedia of Mathematical Sciences*, Vol. 3 (Springer, Berlin, 2006).
[32] G. M. Zaslavsky, *The Physics of Chaos in Hamiltonian Systems* (Imperial College Press, London, 2007).
[33] A. I. Neishtadt, in *Hamiltonian Systems with Three or More Degrees of Freedom*, edited by C. Simo, NATO ASI Series Vol. 533 (Springer, Netherlands, 1999), pp. 193–212.
[34] V. V. Meleshko and G. W. M. Peters, Phys. Lett. A **216**, 87 (1996).